The definitive publisher version is available online at 10.1016/j.ejps.2022.106279

European Journal of Pharmaceutical Sciences 177 (2022) 106279

Contents lists available at ScienceDirect

European Journal of Pharmaceutical Sciences

journal homepage: www.elsevier.com/locate/ejps

Nanoparticle transport and deposition in a heterogeneous human lung airway tree: An efficient one path model for CFD simulations

Md.M. Rahman [a,b], Ming Zhao [a,*], Mohammad S. Islam [c], Kejun Dong [a], Suvash C. Saha [c]

[a] School of Engineering, Design and Built Environment, Western Sydney University, Penrith, NSW 2751, Australia
[b] Department of Mathematics, Faculty of Science, Islamic University, Kushtia 7003, Bangladesh
[c] School of Mechanical and Mechatronic Engineering, University of Technology Sydney, Ultimo, NSW 2007, Australia

ARTICLE INFO

Keywords:
Airflow dynamics (AD)
Heterogeneous vasculature tree
Particle transport and deposition (TD)
Cutting/truncated path model
Drug delivery
Boundary condition

ABSTRACT

Understanding nano-particle inhalation in human lung airways helps targeted drug delivery for treating lung diseases. A wide range of numerical models have been developed to analyse nano-particle transport and deposition (TD) in different parts of airways. However, a precise understanding of nano-particle TD in large-scale airways is still unavailable in the literature. This study developed an efficient one-path numerical model for simulating nano-particle TD in large-scale lung airway models. This first-ever one-path numerical approach simulates airflow and nano-particle TD in generations 0–11 of the human lung, accounting for 93% of the whole airway length. The one-path model enables the simulation of particle TD in many generations of airways with an affordable time. The particle TD of 5 nm, 10 nm and 20 nm particles is simulated at inhalation flow rates for two different physical activities: resting and moderate activity. It is found that particle deposition efficiency of 5 nm particles is 28.94% higher than 20 nm particles because of the higher dispersion capacity. It is further proved that the diffusion mechanism dominates the particle TD in generations 0–11. The deposition efficiency decreases with the increase of generation number irrespective of the flow rate and particle size. The effects of the particle size and flow rate on the escaping rate of each generation are opposite to the corresponding effects on the deposition rate. The quantified deposition and escaping rates at generations 0–11 provide valuable guidelines for drug delivery in human lungs.

1. Introduction

Nanoparticles have been successfully used as multipurpose carrier frameworks for the therapeutic delivery of drugs for treating respiratory illnesses such as lung cancer, cystic fibrosis, and asthma (Sung et al., 2007; Willis et al., 2012). Targeted distribution of drugs reduces the overall dose and the number of adverse effects associated with high levels of systemic drug treatment (Azarmi et al., 2008). As a result, the study of particle transportation and deposition (TD) in human pulmonary airways is essential to the effectiveness of drugs delivered by the aerosol inhalation (Koullapis et al., 2018; Mangal et al., 2017; Nahar et al., 2013; Valiulin et al., 2021).

For the treatment of respiratory illnesses, many nanomedicines and drug delivery systems have been developed. Intravenous injection and inhalational delivery are the most popular methods to deliver therapeutic or diagnostic materials to the lungs (Babu et al., 2013; Lee et al., 2015; Scherließ et al., 2022). Significant research has been done on nanoparticle transport during inhalational delivery (Azarmi et al., 2008; Ruge et al., 2013). However, little investigation has been done on nanoparticle transport in the pulmonary circulation (Sohrabi et al., 2017). Thus, developing an efficient technique for evaluating nanoparticle delivery in human lungs is essential. To achieve this, a detailed investigation of nanoparticle TD in a human lung model, taking into consideration as many as the lung airways as possible, is necessary.

The factors influencing drug carrier distribution in a heterogeneous vasculature tree include particle size, particle density, inhalation flow conditions, and lung geometry (Kim and Iglesias, 1989). Nanoparticles are solid colloidal particles made up of macromolecular material with diameters ranging from 1 to 1000 nm (Kaur et al., 2008). Dissolving, entrapping, or encapsulating the active material can be accomplished with nanoparticles as drug carriers (Singh and Lillard, 2009). Nanoparticles have been explored as drug carriers for a variety of illnesses, including cancer and tuberculosis (TB) (Sung et al., 2007; Yhee et al., 2016). They are also employed in cancer treatment to target tumour

* Corresponding author.
E-mail address: m.zhao@westernsydney.edu.au (M. Zhao).

https://doi.org/10.1016/j.ejps.2022.106279
Received 18 April 2022; Received in revised form 18 July 2022; Accepted 15 August 2022
Available online 17 August 2022

cells, which play a significant role in inflammation and house germs that cause bacterial infections (Alexiou et al., 2006; Barani et al., 2021).

Nanoparticle TD in the extrathoracic area (nasal, oral and pharynx airways) and tracheobronchial lung airways have been investigated through Computational Fluid Dynamics (CFD) (Xi et al., 2012; Zhao et al., 2020). Yu et al. (1996) used a computer model to simulate the deposition of nanoparticles in a single bifurcation airway. They concluded that the inlet condition significantly impacts concentration and flow pattern. Comer et al. (1999) simulated airflow and particle TD in generations 3 to 5 (G3-G5) of a double bifurcation lung geometry based on Weibel's model (Weibel, 1963). Zhang and Kleinstreuer (2004) investigated airflow and nanoparticle ($1 \leq$ nm ≤ 150) deposition in G0 to G3 of a human upper airway model numerically and concluded that turbulence has negligible effects on nanoparticle deposition in the lung model. Islam et al. (2021a) studied polydisperse aerosol particle deposition in the upper airways up to G5 through CFD. The results showed that the diameter of the lung airway reduction significantly affects the particle deposition in the upper lung airway. CFD has been proved a reliable and accurate methodology for estimating the efficiency of local particle deposition in the human lung airways (Ghalati et al., 2012; Rahimi-Gorji et al., 2016; Vachhani and Kleinstreuer, 2021). Using simplified lung models in CFD studies can find fundamental mechanisms of particle TD through reasonable computational time. However, all the studies mentioned above only investigate a limited number of generations. Rahman et al. (2021b) developed an efficient numerical method to study the deposition of microscale aerosol particles in the symmetric lung model over 14 generations. In the model by Rahman et al. (2021b), the G0 to G14 lung model was cut into a number of sections. The particle mass and flow rates satisfy continuity conditions at the interfaces between sections but not the fluid momentum. The results indicated that the microscale aerosol particle deposition also increased when particle size or flow rate increased.

Some researchers have studied particle TD in realistic lung models, which is more complicated than the symmetric lung model (Huang et al., 2021). Russo et al. (2018) conducted CFD simulations of magnetic nanoparticle drug delivery in a patient-specific realistic lung model of G0 to G3. They found that despite the produced magnetic field intensity, only a tiny percentage of the particles reached the respiratory airways. Through CFD simulations, Rahman et al. (2021c) found that 10% of 5 nm particles are deposited in the mouth to G3 airways, allowing over 90% to reach the deeper lung. Dong et al. (2021) recently investigated nanoparticle TD in realistic human airways generation up to G3. They found Brownian diffusion is a dominating particle deposition mechanism for particles below 10 nm. However, the deposition efficiency dropped substantially when the particle size was increased to 100 nm.

Sosnowski (2018) found that particle flow and deposition in the respiratory tract are influenced by particle coagulation, hygroscopic growth, and dry powder inhalation. Kadota et al. (2022) found that the particle deposition is influenced by airway geometry. They also found that small particles are deposited in the lower bronchial tree and large particles are deposited in the upper airways generations (G2-G6). Ahookhosh et al. (2021) studied the micron-sized particle transport and deposition in human lung airways based on various inhalation flow rates using pressurized metered-dose inhalers drug delivery devices. It was found that the particle deposition rate in the right lung is greater than in the left lung. Ahookhosh et al. (2020b) studied the airflow and micron-size particle deposition in realistic human tracheobronchial airways with varying inhalation flow rates. The results showed that more particles are deposited in the extra-thoracic region, and inertial impaction is the dominant deposition mechanism.

Longest and Holbrook (2012) conducted a review on aerosol transport in the respiratory tract. The review indicated that more accurate models need to be developed through contemporaneous experimental and CFD methods. Longest and Xi (2007) investigated nanoparticle deposition in the upper airways using three models: a straight tubular flow field, a 90° tubular bend, and an idealised human oral airway reproduction. The results show that the oral airway model, which combines a Lagrangian model with a user-defined Brownian motion model and a near-wall interpolation approach, is suitable for nanoparticle deposition in the respiratory tract with diameters ranging from 1 to 120 nm. Tian et al. (2011b) developed an individual stochastic path (SIP) model that considers transient and steady-state conditions to predict aerosol dry powder inhalation from the mouth-throat to the tracheobronchial (TB) airways. The findings show that steady-state simulations produced an excellent view of the overall, regional, and local deposition. At the same time, the transient conditions had little effect on deposition in the TB region, starting with the fourth bifurcation. Tian et al. (2011a) investigated an enhanced condensational growth strategy for aerosol particle delivery in a single path bifurcation model from the mouth to the tracheobronchial zone. The findings show that large aerosol droplets (aerodynamic diameters of 2.4–3.3 m) enhance the tracheobronchial B5 region under ECG delivery settings.

All numerical simulations for realistic geometry only consider limited generations to keep computing costs low (Sohrabi et al., 2014). The complexity of realistic lungs make CFD simulation of whole airways completely impossible (Ahookhosh et al., 2020a; Sohrabi et al., 2017; Zhang et al., 2008). Therefore, symmetric lung based on theoretic models have been constructed to represent the lung trees to predict the particle deposition (Kolanjiyil and Kleinstreuer, 2019).

Considering simulating airflow through the G0-G11 airway using CFD, the total number of bifurcations of only G11 is $2^{11} = 2048$. Detailed CFD simulation for such a significant number of airway bifurcations is impossible. This study aims to develop an efficient numerical model to simulate particle deposition in many generations of human lung airways. Instead of predicting all the bifurcations, only two representative bifurcations of each generation is simulated in the numerical model to predict the airflow and particle TD. The deposition efficiency of these two representative bifurcations of each generation is then converted to the deposition efficiency of all the bifurcations of this generation. The continuity of the airflow mass, airflow momentum and the particle numbers are ensured in the numerical model. The details of the numerical method will be presented in Section 3. Using the newly developed numerical method, we investigated the effect of particle size and inhalation airflow rates on the distribution of deposited particles in G0 to G11 airways. The parameters used in the numerical simulations are summarized in Table 1.

2. Numerical methods

2.1. Geometry of the lung model

The simplified (all called theoretical) geometry developed by Xu and Yu (1986) is used to create the three-dimensional (3D) lung model with symmetric and planner lung airways from generation G0 to G13. The bifurcation angle of lung airways is 70°. The rotation angle is considered because the lung airways are assumed to be symmetric and planar (Deng et al., 2018). The extra-thoracic airways are not considered because they are not available in the theoretical lung models (Poorbahrami and Oakes, 2019). Considering the extra-thoracic airways will reduce the number of particles entering lung airways (Xi et al., 2012). Table 2 lists geometric parameters of the theoretical lung airways from

Table 1
Numerical parameters and simulation conditions.

Parameters	Value
Fluid density (kg/m^3)	1.225
Viscosity of fluid (kg/m.s)	1.7894×10^{-5}
Inhalation flow rates (L/min)	15 and 30
Aerosol particle density (kg/m^3)	1100
Particle diameter (nm)	5, 10 and 20
Total number of injected particles	97,200

Table 2
Geometric parameters of lung airways were calculated using Xu and Yu (1986).

Generation (G)	Generation number, n (Z)	Diameter (cm)	Length (cm)
0	1	1.665	12.286
1	2	1.220	4.284
2	4	0.830	1.896
3	8	0.560	0.759
4	16	0.450	1.268
5	32	0.350	1.071
6	64	0.280	0.901
7	128	0.230	0.759
8	256	0.186	0.639
9	512	0.154	0.538
10	1024	0.130	0.460
11	2048	0.109	0.390
12	4096	0.095	0.330
13	8192	0.082	0.271

G0 to G13. We implemented an efficient truncating method to construct an efficient theoretical lung model to explore the fundamental mechanisms of particle TD in a lung model with many generations. A whole human lung has G0 to G23 generations of airways. We simulated G0 to G13 using CFD and analysed the nanoparticle particle TD in G0 to G11 airways. The airway length from G0 to G11 is 93% of the whole lung from G0 to G23. In an airway tree, the number of airway branches of a generation increases with the increase of generation number exponentially. Because of this, G0 to G11 takes 93% of the airway route length but only about 20% of the whole airway volume.

Fig. 1 depicts the 3D heterogeneous pulmonary vascular symmetric lung tree of adults up to generation G11 used in this study. In the complete lung tree, n-th generation has 2^n bifurcations of the lung airways. Simulating the airflow of all generations from G0 to G11 using CFD without any simplification would be prohibitively unaffordable in terms of computing time. Therefore, we only choose two representative bifurcations for each generation to make it affordable to simulate G0 to G11 using CFD, as shown in Fig. 1. The simplification results in a single path lung up to G11 but does not lose geometric features of the human lung.

2.2. Airflow model

The airflow and particle TD in the lung airways are solved using the ANSYS FLUENT software. The Reynolds-averaged Navier-Stokes (RANS) equations are the governing equations for calculating the flow:

$$\frac{\partial \rho}{\partial t} + \frac{\partial}{\partial x_i}(\rho u_i) = 0 \tag{1}$$

$$\frac{\partial}{\partial t}(\rho u_i) + \frac{\partial}{\partial x_j}(\rho u_i u_j) = -\frac{\partial p}{\partial x_i} + \frac{\partial}{\partial x_j}\left[\mu\left(\frac{\partial u_i}{\partial x_j} + \frac{\partial u_j}{\partial x_i}\right)\right] + \frac{\partial}{\partial x_j}\left(-\rho\overline{u'_i u'_j}\right) \tag{2}$$

where t is time, x_i ($i = 1,2$ and 3) are the Cartesian coordinates, $\rho$is the air density, u_i is the fluid velocity in the x_i-direction, p is the fluid pressure, μ is the molecular viscosity. On the right-hand side of Eq. (2), $\rho\overline{u'_i u'_j}$ represents the Reynolds stresses of turbulence.

The realisable k-ε turbulence model is used to simulate the turbulence and calculate the Reynolds stresses. Realisable k-ε turbulence performs better than the standard k-ε turbulence model, including boundary-free shear flows, channel and flat boundary layer flow with and without pressure gradients, rotating homogeneous shear flows, and backwards-facing step flow (Shih et al., 1995). In addition, the realisable k-ε model can correctly calculate the flow of complex lung geometries without the need for a near-wall correction (Fletcher et al., 2021; Massarotti et al., 2021; Rahman et al., 2021b; Tash et al., 2019).

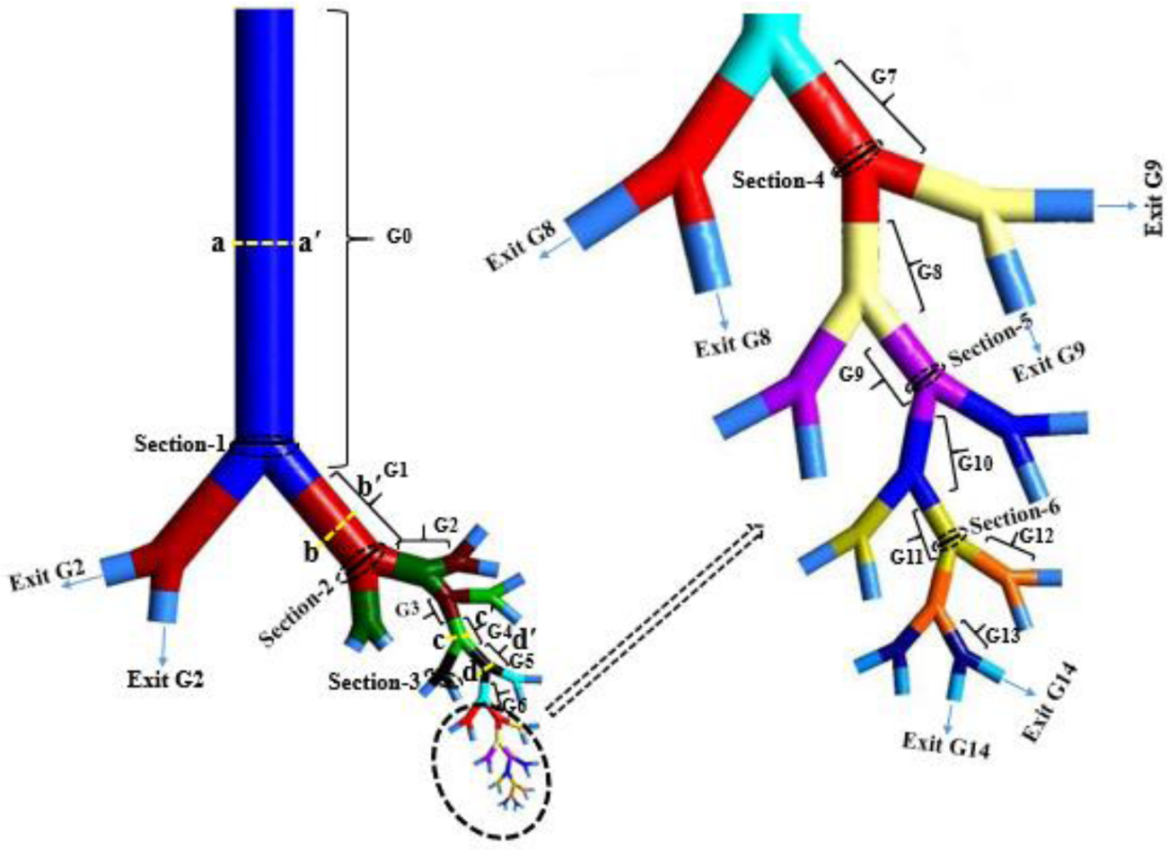

Fig. 1. A model of the adult lung's tracheobronchial airways (G0-G13). When the results are given, the sections indicated in the Figure will be referred to.

2.3. Boundary conditions

The RANS equations are solved using the second-order upwind and pressure-velocity coupling schemes. In some investigations (Bahmanzadeh et al., 2016; Gu et al., 2019), the effects of an unsteady inhalation profile on particle TD were investigated. In the present one path model, only two bifurcations of each generation are retained. Out of these two bifurcations, one is followed by lower generations and one is truncated at the next generation. As a result, there are two exits each truncated bifurcation. In Fig. 1, exit Gn is the cutting position where *n*th generation and following generations are cut off. To ensure the conservation of airflow mass, the airflow rate is assumed to be evenly distributed among all the 2^n bifurcations of the *n*th generation. As a result, the airflow rate of exit Gn is given as $Q_e^n = Q_{in}/2^n$, where Q_{in} is the inlet flow rate at G0. In the numerical simulations, the velocity on each exit is given as:

$$u_n = Q_e^n / A_n \tag{3}$$

where A_n is the cross-sectional area of exit Gn. A reference pressure is specified on the inlet of G0. The airway wall was assumed to be stationary, and the airway wall surfaces were regarded as no-slip surfaces (Farghadan et al., 2020; Rahimi-Gorji et al., 2016).

A trap condition is implemented on the Discrete Phase Model (DPM) airway walls for particle deposition (Inthavong et al., 2011a; Rahman et al., 2022). In the trap condition, particles colliding with the inner surface of the lung airways are trapped. This trap condition is appropriate as the airway walls contain very sticky mucus (Islam et al., 2021c). The escape condition is used in the outlet section for DPM so that the particles can pass through the truncated boundary without being reflected.

2.4. Particle transport model

The current particle TD model is a one-way coupling model that takes into account particle movement driven by airflow but ignores particle impacts on the airflow (Chen et al., 2021; Lintermann and Schröder, 2017). Agglomeration between the particle and water may occur due to external forces such as van der Waals, electrostatic, and capillary forces. The interaction of particles with water is also influenced by air humidity. In this study, agglomeration and air humidity are not considered. However, collision-free conditions can be utilised to simulate particle transport if the density of the particles is low (Tsuji, 2007). Direct particle collision is ignored in this paper because the particles entering the tracheobronchial airway is sufficiently diluted (Feng and Kleinstreuer, 2014; Kadota et al., 2022). Therefore, the dynamics of the particles, such as collision, growth, and aggregation during the particle transportation and deposition into the human lung, were not considered (Deng et al., 2019). The Lagrangian approach is used to describe particle TD in the lung airways. The equation of motion of each particle is expressed as (Inthavong et al., 2011b; Rahman et al., 2021a):

$$\frac{d\boldsymbol{u}_i^p}{dt} = \boldsymbol{F}_{Di} + \boldsymbol{F}_{gi} + \boldsymbol{F}_{Bi} + \boldsymbol{F}_{Li} \tag{4}$$

where u_i^p is particle velocity in the x_i-direction, $\boldsymbol{F}_{\text{Di}}$, $\mathbf{F}_{\text{gi}}$, $\boldsymbol{F}_{\text{Bi}}$ and $\boldsymbol{F}_{\text{Li}}$ are the drag force, gravitational force, Brownian force, and Saffman's lift force per unit mass. The following formula determines the gravitational force:

$$\boldsymbol{F}_{gi} = \left(\frac{\rho_p - \rho}{\rho}\right)\boldsymbol{g} \tag{5}$$

where $\boldsymbol{g}$ denotes gravitational acceleration and $\rho_p$denotes particle density. The drag force is calculated using the following formula:

$$\boldsymbol{F}_{Di} = \frac{18\mu}{\rho_p d_p^2} C_D \frac{Re_p}{24}\left(\boldsymbol{u}_i - \boldsymbol{u}_i^p\right) \tag{6}$$

where $Re_p = \rho d_p \left|\boldsymbol{u}_i^p - \boldsymbol{u}_i\right|/\mu$ and the drag coefficient C_D for the spherical particles is calculated by

$C_D = a_1 + \frac{a_2}{Re_p} + \frac{a_3}{Re_p^2}$ for $0 < Re_p < 10$ (Morsi and Alexander, 1972), where a_1, a_2, a_3 are functions of the Reynolds number Re_P given by:

$$a_1,\ a_2,\ a_3 = \begin{cases} 0,\ 24,\ 0 & 0 < R_e < 0.1 \\ 3.690,\ 22.73,\ 0.0903 & 0.1 < R_e < 1 \\ 1.222,\ 29.17,\ 3.89 & 1 < R_e < 10 \\ 0.617,\ 46.50,\ -116.67 & 10 < R_e < 100 \\ 0.364,\ 98.33,\ -2778 & 100 < R_e < 1000 \\ 0.357,\ 148.62,\ -47500 & 1000 < R_e < 5000 \\ 0.46,\ -490.546,\ 578700 & 5000 < R_e < 10000 \\ 0.519,\ -1662.5,\ 5416700 & R_e > 10000 \end{cases}$$

When particles interact with a fluid, Brownian motion describes particles' random, uncontrolled movement (Grassia et al., 1995). It is prominent when small size particles are in a fluid with small viscosity and high temperature (Jang and Choi, 2004). If the particle size is more than 1 μm, Brownian motion in the air is undetectable (Hou et al., 1990). The Brownian force is calculated by:

$$\boldsymbol{F}_{Bi} = \boldsymbol{G}_i \sqrt{\frac{\pi S_0}{\Delta t}} \tag{7}$$

where G_i is a Gaussian random number with unit variance and zero mean, Δt is the particle time step, and S_0 is the spectral intensity function associated with the diffusion coefficient by:

$$S_0 = \frac{216\nu k_B T}{\pi^2 \rho_p d_p^2 \left(\frac{\rho_p}{\rho}\right)^2 C_c} \tag{8}$$

where, ν is the kinematic viscosity, $K_B = 1.380649 \times 10^{-23}$ J/K is the Boltzmann constant,$T = 300K$ is the absolute fluid temperature, and C_c is the Stokes-Cunningham slip correction coefficient as defined by:

$$C_c = 1 + \frac{2\lambda}{d_p}\left(1.257 + 0.4e^{-\left(\frac{1.1 d_p}{2\lambda}\right)}\right) \tag{9}$$

where, the gas molecule mean free path (λ) is 65 nm (Xi et al., 2012). The lift force of Saffman is calculated using the following formula:

$$\boldsymbol{F}_{Li} = \frac{2K\nu^{\frac{1}{2}}\rho d_{ij}}{\rho_p d_p (d_{lk} d_{kl})^{\frac{1}{4}}}\left(\boldsymbol{u}_j - \boldsymbol{u}_j^p\right) \tag{10}$$

where, $K = 2.594$ is the constant coefficient of Saffman's lift force and $d_{ij} = (\partial u_i/\partial x_j - \partial u_j/\partial x_i)/2$ is the deformation tensor of the flow velocity.

2.5. Deposition efficiency calculation

The deposition efficiency of *n*-th generation is defined as the proportion of particles absorbed (trapped) in this generation of airways out of the particles released at the inlet boundary and is denoted by η_n where the subscript n stands for *n*-th generation.

$$\eta_n = \frac{2^n N_n}{N} \tag{11}$$

where N_n is the number of particles deposited at each bifurcation of n-th generation and N is the total number of particles released on the inlet of G0. In Fig. 1, each generation has two bifurcations, and N_n is the averaged numbers of deposited particles deposited at these two bifurcations. The particle escaping rate at the n-th generation is defined as the percentage of particles that enter deeper lung at all the bifurcations of this generation, and it is calculated as:

$$e_n = 1 - \sum_{i=1}^{n} \eta_i \tag{12}$$

3. Grid dependency study and model validation

3.1. Grid dependency study

The computational mesh of the symmetric lung airways is shown in Fig. 2. Ten-layer smooth inflation was implemented near the walls to ensure that the boundary layer flow was correctly represented (Fig. 2a). In addition, the denser mesh is used at carinal angles for the proper resolution of complicated flows.

The grid independence test is conducted by performing numerical simulations with six meshes, Mesh-1 to Mesh-6, whose element numbers range from 338,349 to 1,908,633. While the mesh size is inversely proportional to the element number, the densest mesh has the smallest grid size of 0.11 mm. In that situation, asymmetric flow distributions appear when the flow passes in the truncated branch. To ensure the continuity of the airflow rate, we use the mass flow rate at each truncated outlet to guarantee that the velocity is distributed uniformly. The air is sucked in the lung through the inlet by the low pressure of the lung. As a result, the velocity follows a naturally developed velocity profile as shown in Fig. 3(b). It can be found that the velocity profile at the inlet face is nearly parabolic, with an increase in the element number shown in Fig. 3(b). Line 1 and 2 in Fig. 3(a) are near the end of the flow path and chosen because the flow at these two lines is sensitive to any numerical errors along the air flow route. Therefore, velocities on section-7 and lines 1 and 2 indicated in Fig. 3(a) are evaluated. Fig. 3(e) show the average velocity at section 7, and Fig. 3(c,d) shows the velocity distribution along two lines 1 and 2, where X denotes the direction along the line. As shown, increasing the node number has a negligible effect on the velocity if the mesh density exceeds Mesh-4. The maximum velocity difference between Mesh-5 and Mesh-6 is 0.011%. As a result, the velocity at Mesh-5 is used for all the simulations.

The non-dimensional wall unit (y^+) is defined inside the boundary layer as

$$y^+ = \frac{\rho U_\tau y}{\mu} \tag{13}$$

where $U_\tau \left(= \sqrt{\frac{\tau_w}{\rho}}\right)$ is the friction velocity, y is the distance the first layer of mesh to the wall, and τ_w is the shear stress on the wall, the value of y and y^+ for Mesh-5 are 0.117 mm and 1.48, respectively.

Fig. 4(a) depicts the effect of mesh element number on deposition efficiency. The deposition efficiency remains nearly unchanged after increasing the mesh density above Mesh-4 (1.07 million elements). All numerical simulations in this investigation employed Mesh-5, which has 1.43 million elements. To show that sufficiently large number of particles have been released, simulations are repeatedly conducted by releasing different numbers of particles on the inlet. Fig. 4(b) demonstrates how the G0-G11 lung model's deposition efficiency varies with the number of particles released at the inlet. If the number of particles released exceeds 64 000, the deposition efficiency is unaffected by the particle number. Fig. 4(b) proves that the particle number of 97,200 used in this paper is large enough to produce converged results.

3.2. Model validation

In our previous study (Rahman et al., 2021a), we have already conducted the validation of particle TD of nanoparticles in human lung airways with the limited number of generations G3-G5. To further validate the proposed one path model in the simulation of TD of nanoparticles, we simulated the flow and particle TD in G6 to G7 using the completed G6-G7 model in Fig. 5(a) and one path G6-G7 model in Fig. 5 (b). Two bifurcations of G8 have been cut off in Fig. 5(b). The details of the deposition efficiencies for the whole G6-G7 model and one path G6-G7 model are compared with each other in Table 3. It can be found that the present CFD results of the one-path model are very similar to the whole model, with a maximum difference of 0.681% occurring at G7 and d_p = 20 nm. Assuming this maximum error of 0.681% at each generation, simulating particle deposition with G0 to G11 will have a maximum error of about 0.681% × 11 = 7.5%. With this maximum error, the proposed one-path model enables the simulation of particle TD in many generations to be performed.

4. Results and discussion

The airflow dynamics and particle deposition are analysed under two flow conditions: low-level breathing (Q_{in} =15 L/min) at rest and

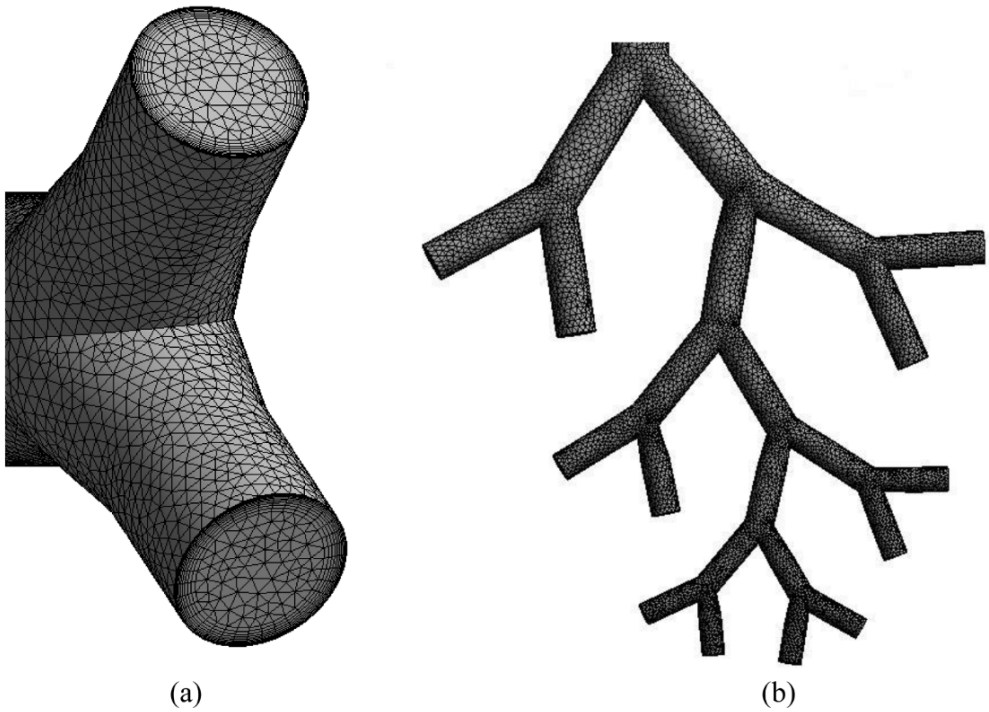

Fig. 2. Computational mesh; (a) Refined mesh near the airway wall; (b) Mesh resolution on the inner wall of G7 to G11 airways.

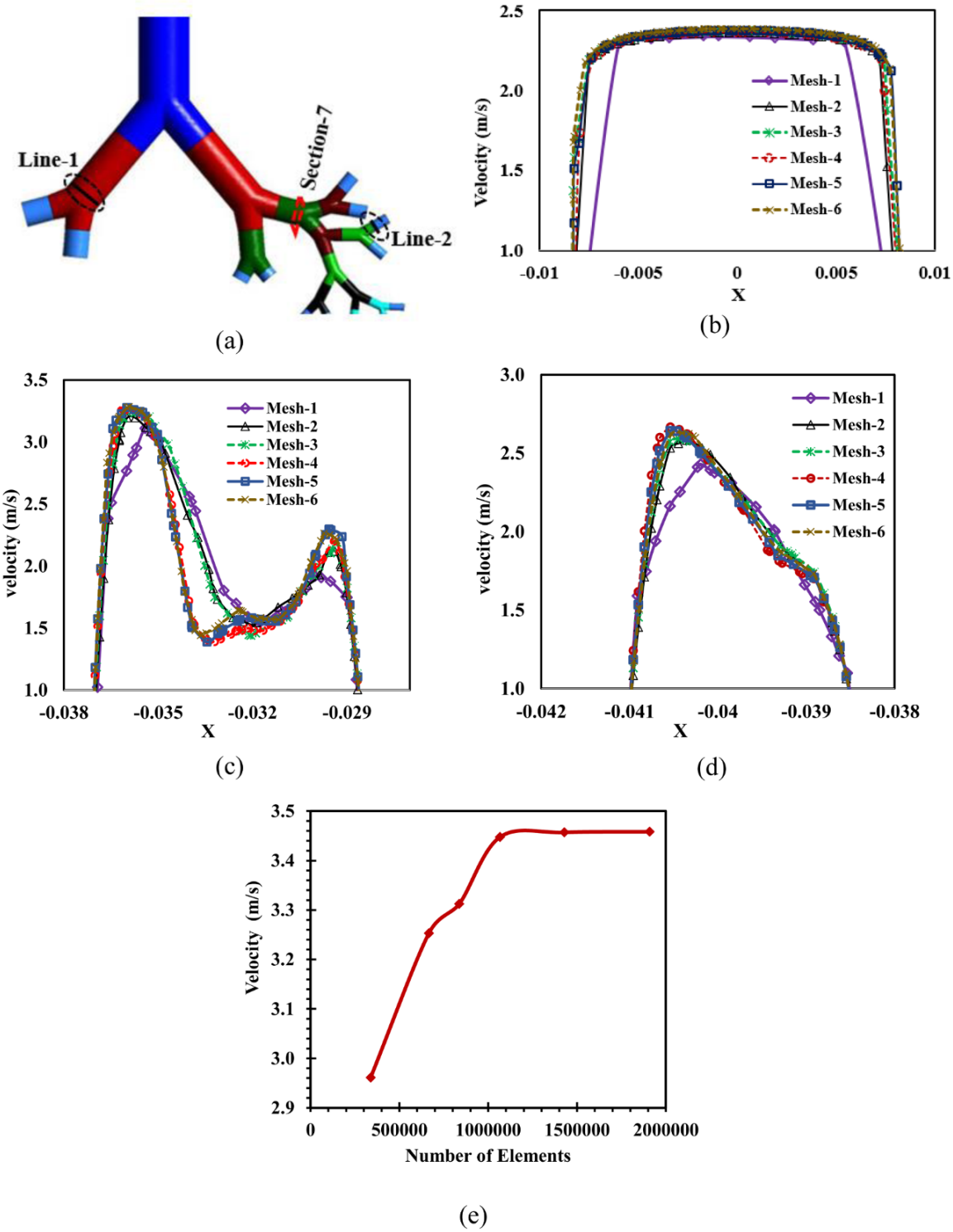

Fig. 3. Grid independent test at flow rate 30 L/min in generations G0-G4. (a) Definition of sections and lines; (b) Velocity distribution at inlet face; (c) Velocity distribution at Line-1; (d) Velocity distribution at Line-2 (average velocity calculated at the selected line in Fig. 3a); (e) Average velocity as a function of grid number.

moderate activity breathing (Q_{in} = 30 L/min) during walking (Gorji et al., 2013; Zhang and Kleinstreuer, 2003). The sizes of medicine particles are generally in the range of 1 nm $\leq d_p \leq$ 1000 μm (Singhal et al., 2016). Solid colloidal particles with a diameter between 1 and 1000 nm are the most typical definition of nanoparticles used for drug delivery (Dailey et al., 2006; De Jong and Borm, 2008; Kreuter, 1991; Sung et al., 2007). However, some researchers argued that nanoparticles in the 50 - 500 nm (Uchechi et al., 2014) and 1–200 nm (Mansour et al., 2009) are suitable for drug delivery. Moreover, most existing studies considered nanoparticles as a drug delivery range of 1 nm $\leq d_p \leq$ 100 nm (Bahrami et al., 2017; Kong et al., 2017; Sun et al., 2021). Therefore, nanoparticles TD of particles with diameters in the range of 5 nm $\leq d_p \leq$ 20 nm are considered in this study.

4.1. Airflow characteristics

Fig. 6 depicts airflow velocity profiles on the symmetric plane within the lung generations up to G13. In the numerical simulations, the conservation of mass is ensured by specifying flow rates at all the exits. Fig. 6 shows very uneven velocity distribution near each bifurcation.

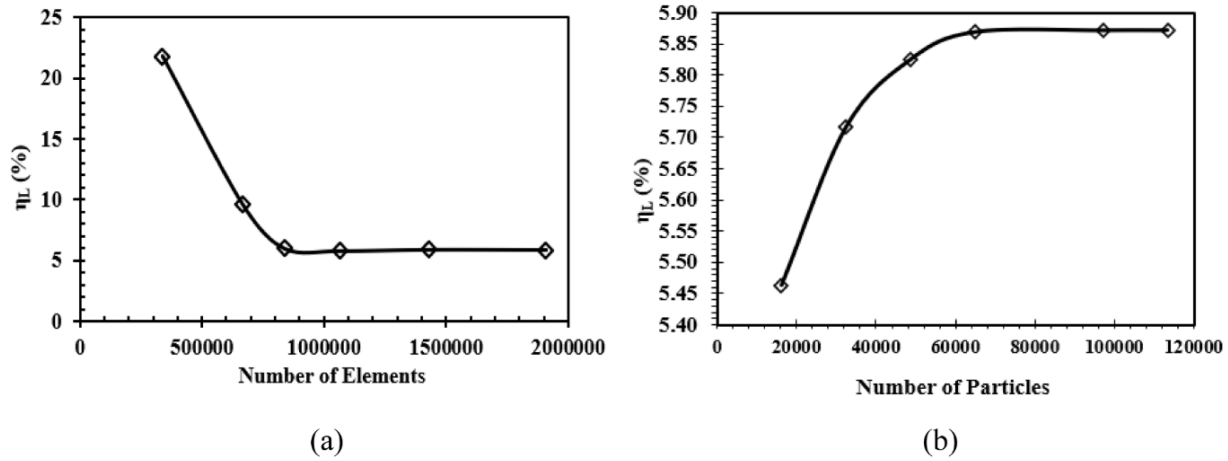

Fig. 4. Shows (a) Deposition efficiency as a function of grid number, (b) Deposition efficiency as a function of released particles number, at generations G0 to G11 at the flow rate of 30 L/min and aerosol particle diameter of 20 nm.

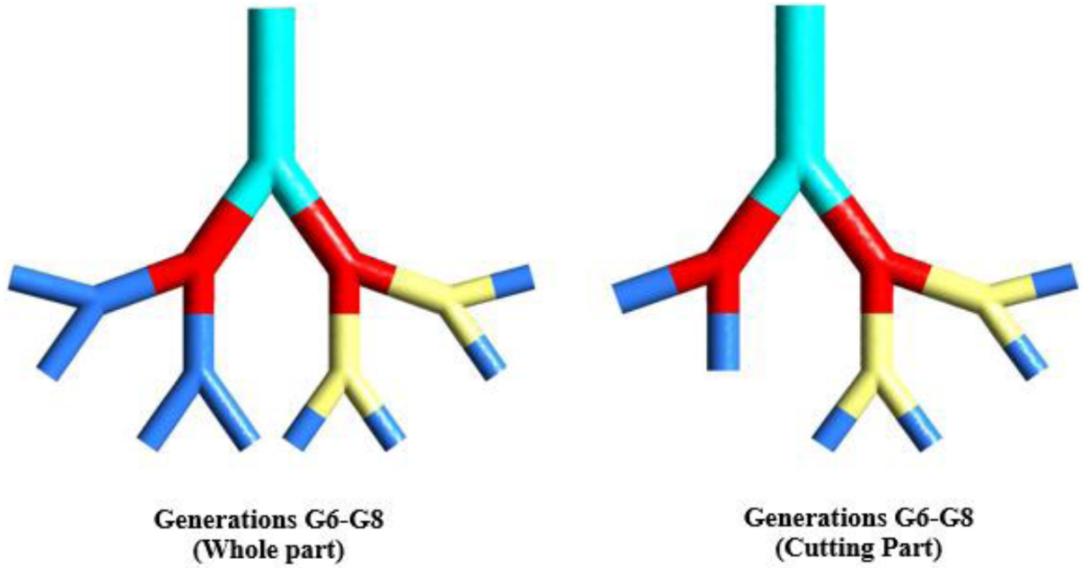

Fig. 5. Comparison of the deposition efficiency results for the current simulation cutting method with the whole G6-G8 model.

Table 3
Local particle deposition efficiency comparison.

Particle size	Local Particle Deposition Efficiency, η_L (%)								
	Whole part model (G6-G9)			Cutting part model (G6-G9)			Difference (%)		
	G6	G6	G6	G6	G6	G8	G6	G7	G8
5 nm	47.986	18.653	7.027	47.831	18.531	7.013	0.323	0.654	0.209
10 nm	33.153	10.639	4.806	33.047	10.584	4.798	0.320	0.514	0.168
20 nm	17.486	5.833	2.847	17.456	5.794	2.839	0.171	0.681	0.276

After air passes through each bifurcation, its velocity accelerates locally on one side and reduces at another side of each airway. The distribution patterns of the velocity in the airways for the two flow rates are similar to each other in Fig. 6. The distribution of the velocity near each bifurcation in Fig. 6 is in a same pattern as that reported by Mutuku and Chen (2018). After each airway is split into two, air flow velocity is accelerated at the inner airway walls that face the incoming flow.

The airflow distribution in airways is further explored using velocity profiles at various sections in the upper airway regions in Fig. 7. The averaged velocity at the inlet u_0 is used for non-dimensional velocity. Because of the difference in the Reynolds number, the non-dimensional velocity distributions along each line in Fig. 7 of two flow rates follow a similar pattern but are not identical. The non-dimensional velocity profile on *aa'* line in the upper airway is symmetrical before the air enters the first bifurcation. After G1, however, velocities varied significantly because of the complexity of airway geometry. The velocity on one side of *bb*' is significantly higher than the other side. In addition, the velocity distribution in the lung airways of different generations are very different from each other. For example, the velocity of G1 (bb') are very different from that of G5 (cc'). The most unevenness of the velocity is found to be at section *bb'*.

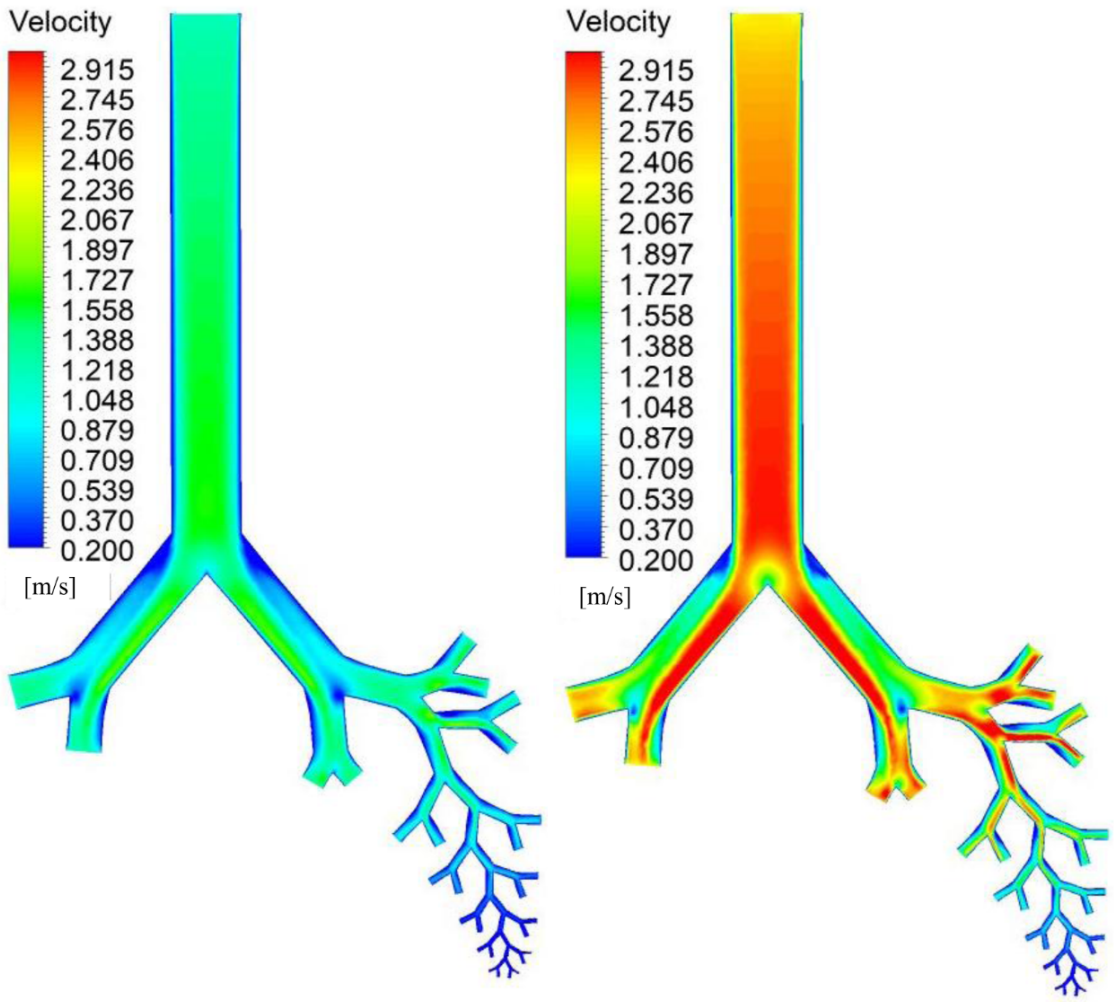

(a) Q_{in}=15 L/min (b) Q_{in}=30 L/min

Fig. 6. Velocity contours for different flow rates at the lung airways generation (G0–G13); (a) Q_{in}=15 L/min; (b) Q_{in}=30 L/min.

4.2. Wall shear stress

It is understandable that the shear stress increase with the increase in flow rate. Because different flow rates have different Reynolds number, the shear stress will not be linearly proportional to the square of the velocity. The non-dimensional shear stress defined by $(\tau / (\rho u_0^2))$ can easily quantify the shear stress relative to the incoming flow velocity. Fig. 8 shows the averaged non-dimensional shear stress $(\tau / (\rho u_0^2))$ at six sections indicated in Fig. 1 along the airflow route, where wall shear stress τ on each section is averaged shear stress over the circumference of this section. The variations of the wall shear stress along the airflow route for the two flow rates follow a similar trend. However, the non-dimensional wall shear stress at Q_{in} = 15 L/m is significantly greater than that at Q_{in} = 30 L/min because the contribution of viscosity decreases with the increase of the Reynolds number.

The non-dimensional pressure distribution along the lung airways at six different locations are shown in Fig. 9, where the locations are indicated in Fig. 1. The pressure decreases with the increase of distance from the inlet of G0, i.e. the deeper a location in the lung, the lower the pressure. Based on Bernoulli's theory and neglecting the potential energy, the velocity decreases as the air enters the deep lung, which is also demonstrated in Fig. 6. The air pressure decreases as air goes into the deep lung mainly because the airflow overcomes much resistance from the friction caused by the viscosity of the flow.

4.3. Particle deposition

The effects of flow rate and particle size on global particle deposition efficiency in lung airway generations G0-G11 are depicted in Fig. 10. The deposition efficiencies of all three particle sizes decrease with increased flow rates at every generation in Fig. 10 because the diffusion mechanism weakens. The deposition efficiency of 5 nm particles in each generation is significantly higher than those of 10 and 20 nm particles. At Q_{in} = 15 L/min, 24.92%, 12.50% and 4.10% of 5 nm, 10 nm and 20 nm particles are deposited at G0, respectively, in Fig. 10(a). When the flow rate is increased to 30 L/min, the deposition efficiencies of 5 nm, 10 nm and 20 nm at generation G0 are reduced to 17.21%, 7.29% and 1.67%, respectively, compared with the flow rate of 15 L/min. Moreover, 9.58% of 5 nm, 4.93% of 10 nm and 2.09% of 20 nm particles are deposited at the generation G11 at flow rate Q_{in} = 15 L/min, while 8.44% of 5 nm, 4.75% of 10 nm and 1.72% of 20 nm particles are deposited at the same generation at Q_{in} = 30 L/min.

It has been proved that the deposition of nanoparticles in human lungs are mainly dominated by the Brownian diffusion and Saffman lift force (Inthavong et al., 2011b; Kleinstreuer et al., 2008). The combined Brownian diffusion and Saffman lift force are called diffusion mechanisms in this paper since they contribute to particle motion in the crossflow direction. The diffusion mechanism weakens with the increase of particle size and flow rate (Dong et al., 2019; Islam et al., 2021b). The contribution of the impaction mechanism to the deposition of nanoparticles is weak because drag forces on particles are strong. Without

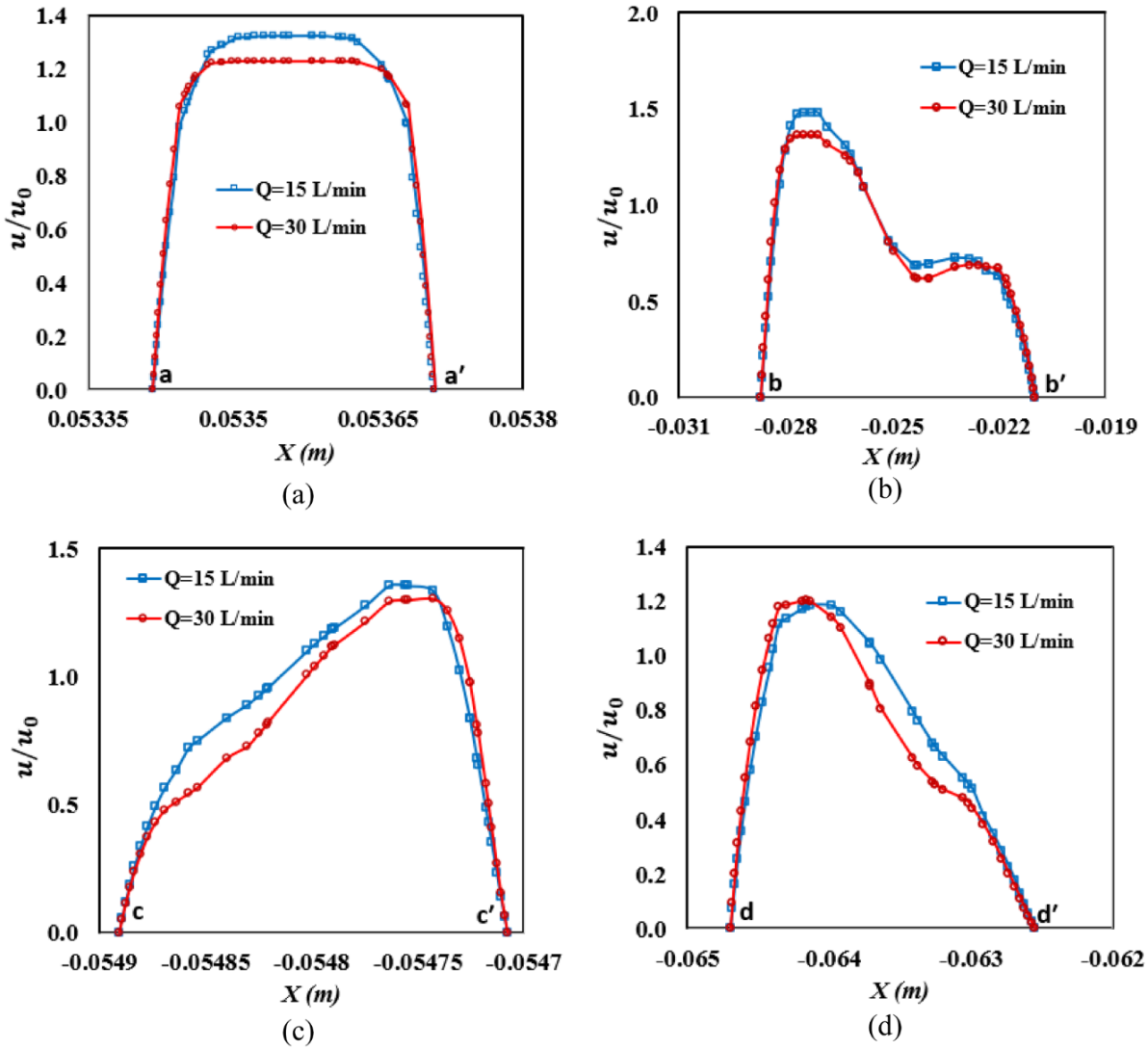

Fig. 7. Velocity profiles at various flow rates, (a) Line aa', (b) Line bb', (c) Line cc', and (d) Line dd' (Fig. 1 illustrates the locations of these lines).

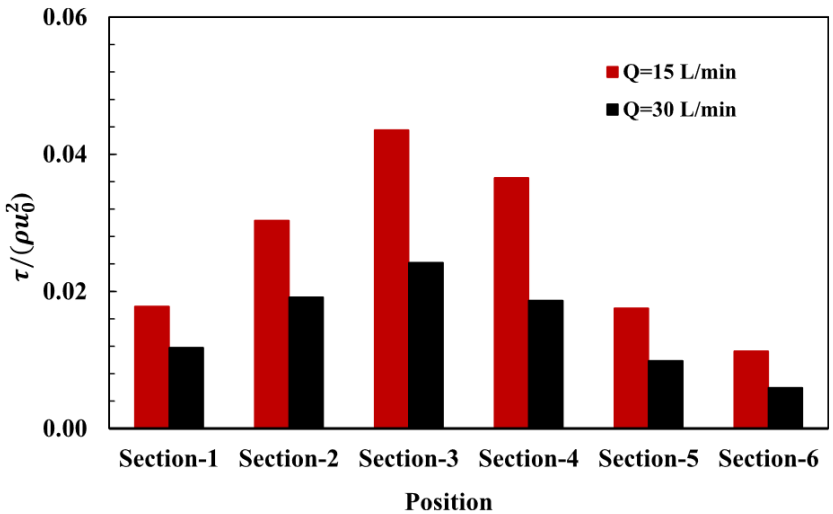

Fig. 8. Averaged wall shear stress for a particular lung portion is indicated in Fig. 1.

diffusion mechanism strong drag forces make particles follow to the outlet and cause no deposition. Fig. 10 indicates that a drop in flow rate increases the deposition efficiency of nanoparticles because reduced flow velocity provides particles a longer time to travel in the crossflow direction towards the wall (Darquenne, 2020).

The difference between the deposition efficiencies at 30 L/min and 15 L/m decreases with increasing particle size. In Fig. 10(c), the ratio $\eta_{d,\ 30\ L/min}/\eta_{d,\ 15\ L/min}$ further illustrates the effect of the flow rate on the

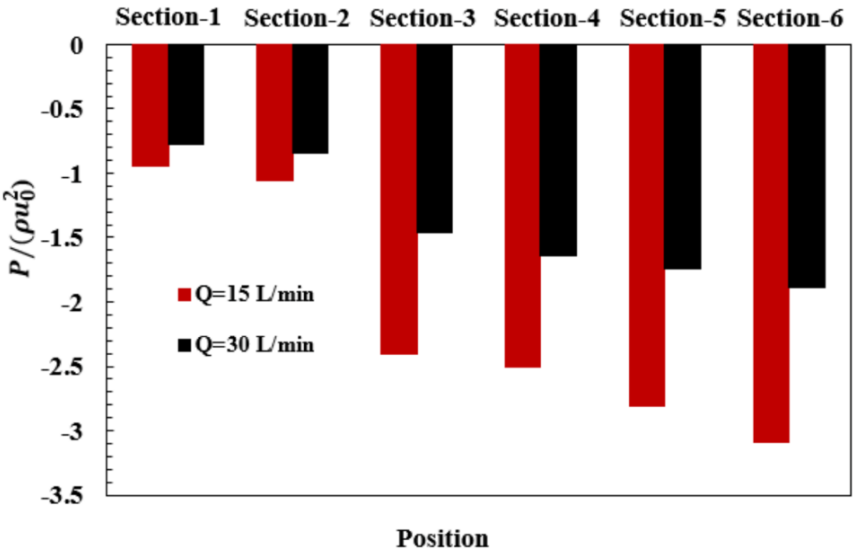

Fig. 9. Pressure drop at two distinct flow rates in a different section of the lung model; the section numbers are shown in Fig. 1.

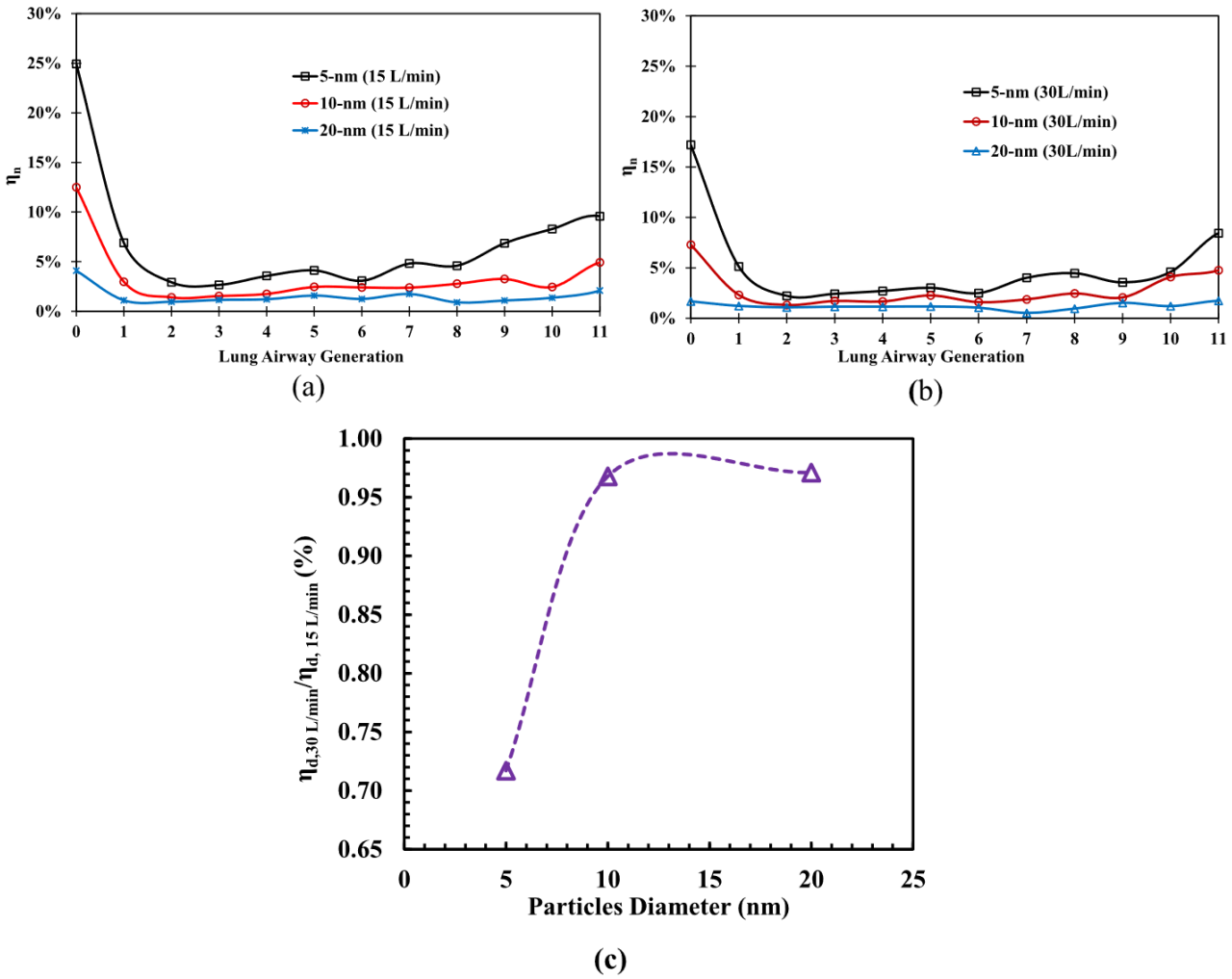

Fig. 10. Particle deposition efficiency in airway lung generation: (a) Q_{in} = 15 L/min; (b) Q_{in} = 30 L/min; (c) Ratio of the deposition rates at the two flow rates.

deposition rate. When the particle size is 20 nm, $\eta_{d,\ 30\ L/min}/\eta_{d,\ 15\ L/min}$ is 0.97, indicating that the flow rate has very weak effect on the deposition efficiency. The effects of flow rate decrease with decreasing particle size. The variation of the deposition efficiency with the generation number in Fig. 10 follows similar trend that was reported by Sohrabi et al. (2017), who used a single route model to increase the efficiency of the numerical simulations.

4.4. Visualisation of particle deposition

Fig. 11 shows the visualisation of the local particle distribution of different sized particles at generation G0-G11 at the flow rate of 15 L/min. The calculated total deposition efficiency of G0 to G11 of 5 nm, 10 nm and -20 nm particles are 36.88%, 18.73% and 7.94%, respectively. Because of the higher dispersion capacity, the 5 nm particles have much higher deposition efficiency than 20 nm particles at Generation G0-G11. As a result, the deposited 5 nm particles are much more evenly distributed in all the airways than 20 nm particles, as shown in Fig. 11(a, b). In addition to stronger Brownian diffusion mechanism, smaller particles also receive a stronger lift force than bigger particles, which contributes to the particle motion in the crossflow direction. As a result, particles can move in the crossflow direction and reach the inner airway wall even if the airway is vertically straight at G0.

It has been proved that the diffusion of microscale particles is dominated by the impaction mechanism (Shi et al., 2007). Under the impaction mechanism, particles are deposited in the wall surface where the velocity is amplified (Rahman et al., 2021c); as a result, the velocity distribution is significantly correlated to the deposited particle distribution along the lung airway wall. However, it can be seen that the distribution pattern in the airway in Fig. 11 is not correlated to the velocity. For example, the area where the velocity is high in Fig. 6 does not necessarily have large deposition in Fig. 11. It appears that, the deposited particles are evenly distributed along the circumference on each section of an airway. This further prove that deposition of nanoparticles are dominated by diffusion instead of impaction.

4.5. Particle escaping rate

The percentage of particles that escape from the outlets each generation and enter the deep lung is known as the escaping rate (defined as e_n). The rate of escape from all exits of a generation is equal to $1 - \eta_n$, where η_n represent the deposition efficiency of all bifurcation of this generation. The percentage of particles that can escape G11 and reach generations after G12 is known as the escape rate at G11. Particle size has the opposite impact on escape rate as it has on deposition rate. Fig. 11 quantifies the escape rate at generations G0-G11 for two flow rates. The escape rate reduces as the generation increases because of particle deposition on the upper lungs. At both flow rates, the escape rate of 5 nm particles at every generation is much lower than that of 20 nm particles.17.68% and 39.77% of 5 nm particles can pass G11 and go into the deeper lung airways for flow rates 15 L/min and 30 L/min, respectively (Fig. 12). At 15 L/min, the escaping rates of 10 nm and 20 nm particles at G11 are 59.15% and 81.42%, respectively. As the flow rate is increased to 30 L/min, the escaping rates of 10 nm and 20 nm particles at generation are increased to 66.60% and 85.62%, respectively. Hence, the particle escape rate increases with the increase of the flow rate.

5. Conclusion

This paper presents a new one path numerical model for simulating particle deposition in human lungs with a reasonable computational effort and investigates the deposition in generations G0 to G11 using the method. We develop a correlation to convert local deposition efficiency to global deposition efficiency for all the generations. Furthermore, the effects of the particle size and the inhaled air flow rate on the deposition efficiency are studied. The key conclusions are summarized below.

- Non-dimensional velocity distributions in lung of the two flow rates follow a similar trend, but not the same because of the difference in the Reynolds number.
- More pressure drop is observed at the flow rate of 30 L/min compared to 15 L/min. It was observed that average pressure drops of 38.32% at a flow rate of 30 L/min compared to a flow rate of 15 L/min because the volume flow rate decreases.
- The particle size affects the distribution of the deposited particles in different generations of the lung. However, the majority of nanoparticles are deposited in the G0 generation.
- 5 nm particle is more evenly distributed than 20 nm particles (Fig. 11) because the diffusion effect increases with the reduction in the particle size and is not affected by the geometry of the airways. Therefore, the diffusion is strong when the particle size is small.

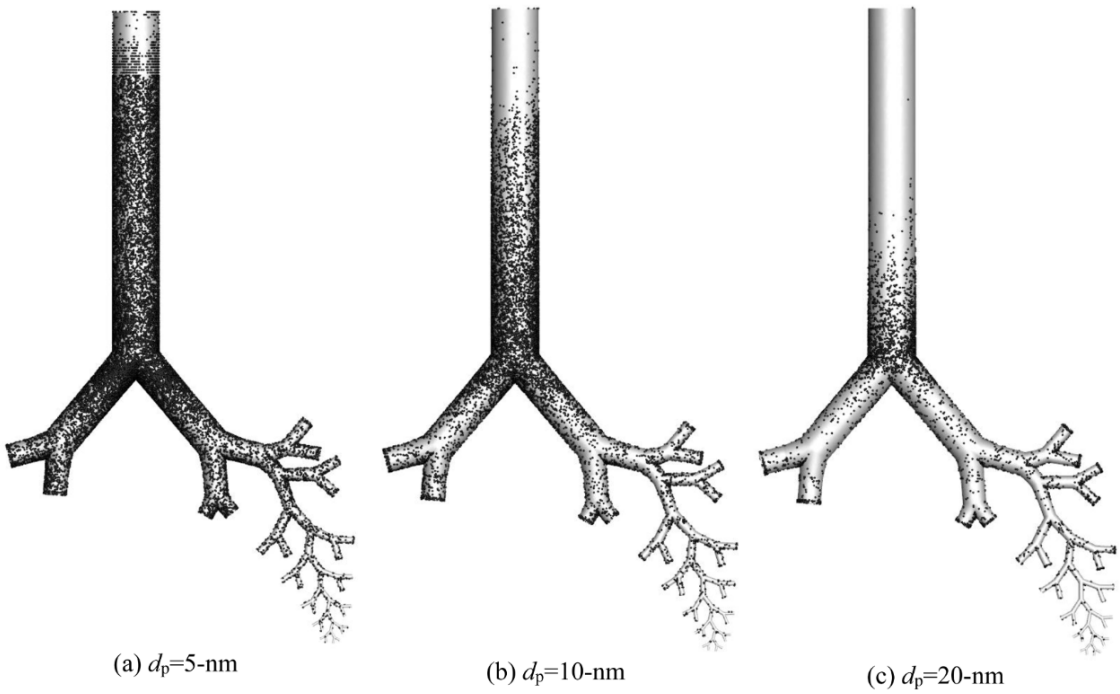

Fig. 11. shows the distribution of deposited particles in human lung airways at flow rates of 15 L/min: (a) 5 nm particles, (b) 10 nm particles, and (c) 20 nm particles.

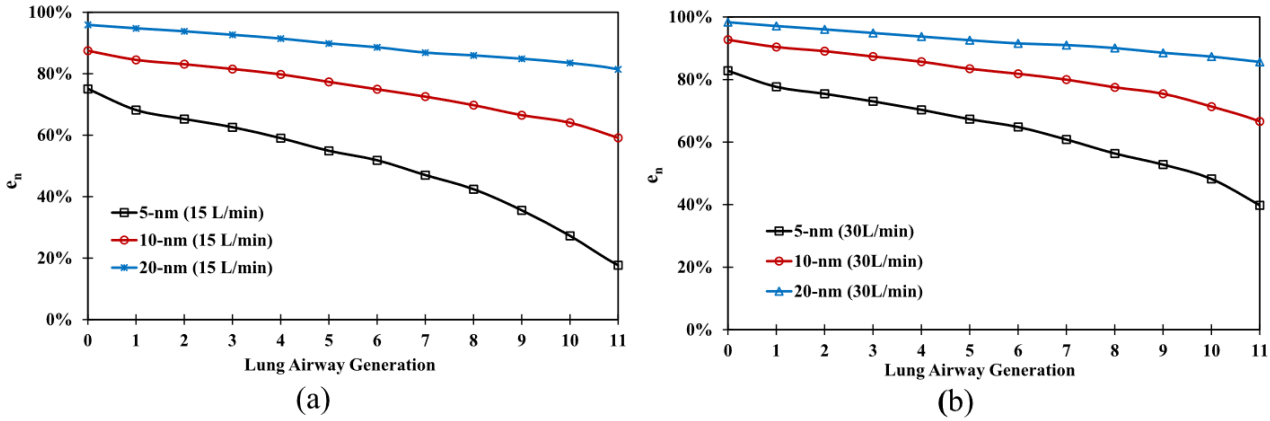

Fig. 12. Escape rates (e_n) for 5 nm $\leq d_p \leq$ 20 nm particles at different flow rate: (a) Q_{in} = 15 L/min; (b) Q_{in}=30 L/min.

- Particles with a small diameter and small flow rate are more deposited in the upper lung airways.
- The total particle deposition efficiency of 5 nm and 20 nm at flow rate Qin = 15 L/min is 36.88% and 7.94%, respectively. Therefore, the 5 nm particles have much higher deposition efficiency than 20 nm because of the higher dispersion capacity.
- The analysis of the escaping rates for nanoparticles shows that more particles enter the deep lung with a high flow rate. Therefore, the findings are crucial for treating lung diseases that affect the deep lung airways.

CRediT authorship contribution statement

Md.M. Rahman: Investigation, Conceptualization, Methodology, Validation, Writing – original draft, Formal analysis. **Ming Zhao:** Supervision, Conceptualization, Methodology, Writing – review & editing. **Mohammad S. Islam:** Conceptualization, Writing – review & editing, Supervision. **Kejun Dong:** Writing – review & editing, Supervision. **Suvash C. Saha:** Writing – review & editing, Supervision.

Declaration of Competing Interest

The authors state no conflict of interest.

Acknowledgments

Mr Rahman acknowledges the support of the Australian Government Research Training Program's International Postgraduate Research Scholarship (IPRS). The authors also acknowledge that the WSU High-Performance computer provided the computational facilities.

References

Ahookhosh, K., Pourmehran, O., Aminfar, H., Mohammadpourfard, M., Sarafraz, M.M., Hamishehkar, H., 2020a. Development of human respiratory airway models: a review. Eur. J. Pharm. Sci. 145, 105233.
Ahookhosh, K., Saidi, M., Aminfar, H., Mohammadpourfard, M., Hamishehkar, H., Yaqoubi, S., 2020b. Dry powder inhaler aerosol deposition in a model of tracheobronchial airways: validating CFD predictions with *in vitro* data. Int. J. Pharm. 587, 119599.
Ahookhosh, K., Saidi, M., Mohammadpourfard, M., Aminfar, H., Hamishehkar, H., Farnoud, A., Schmid, O., 2021. Flow structure and particle deposition analyses for optimization of a pressurized metered dose inhaler (pMDI) in a model of tracheobronchial airway. Eur. J. Pharm. Sci. 164, 105911.
Alexiou, C., Schmid, R.J., Jurgons, R., Kremer, M., Wanner, G., Bergemann, C., Huenges, E., Nawroth, T., Arnold, W., Parak, F.G., 2006. Targeting cancer cells: magnetic nanoparticles as drug carriers. Eur. Biophys. J. 35, 446–450.
Azarmi, S., Roa, W.H., Löbenberg, R., 2008. Targeted delivery of nanoparticles for the treatment of lung diseases. Adv. Drug Deliv. Rev. 60, 863–875.
Babu, A., Templeton, A.K., Munshi, A., Ramesh, R., 2013. Nanoparticle-based drug delivery for therapy of lung cancer: progress and challenges. J. Nanomater. 2013, 863951.
Bahmanzadeh, H., Abouali, O., Ahmadi, G., 2016. Unsteady particle tracking of micro-particle deposition in the human nasal cavity under cyclic inspiratory flow. J. Aerosol Sci. 101, 86–103.
Bahrami, B., Hojjat-Farsangi, M., Mohammadi, H., Anvari, E., Ghalamfarsa, G., Yousefi, M., Jadidi-Niaragh, F., 2017. Nanoparticles and targeted drug delivery in cancer therapy. Immunol. Lett. 190, 64–83.
Barani, M., Mukhtar, M., Rahdar, A., Sargazi, G., Thysiadou, A., Kyzas, G.Z., 2021. Progress in the application of nanoparticles and graphene as drug carriers and on the diagnosis of brain infections. Molecules 26, 186.
Chen, W.H., Chang, C.M., Mutuku, J.K., Lam, S.S., Lee, W.J., 2021. Analysis of microparticle deposition in the human lung by taguchi method and response surface methodology. Environ. Res. 197, 110975.
Comer, J., Kleinstreuer, C., Hyun, S., Kim, C., 1999. Aerosol transport and deposition in sequentially bifurcating airways. J. Biomech. Eng. 122, 152–158.
Dailey, L., Jekel, N., Fink, L., Gessler, T., Schmehl, T., Wittmar, M., Kissel, T., Seeger, W., 2006. Investigation of the proinflammatory potential of biodegradable nanoparticle drug delivery systems in the lung. Toxicol. Appl. Pharmacol. 215, 100–108.
Darquenne, C., 2020. Deposition mechanisms. J. Aerosol. Med Pulm. Drug Deliv. 33, 181–185.
De Jong, W.H., Borm, P.J., 2008. Drug delivery and nanoparticles: applications and hazards. Int. J. Nanomed. 3, 133.
Deng, Q., Deng, L., Miao, Y., Guo, X., Li, Y., 2019. Particle deposition in the human lung: health implications of particulate matter from different sources. Environ. Res. 169, 237–245.
Deng, Q., Ou, C., Chen, J., Xiang, Y., 2018. Particle deposition in tracheobronchial airways of an infant, child and adult. Sci. Total Environ. 612, 339–346.
Dong, J., Li, J., Tian, L., Tu, J., 2021. Transport and deposition of ultrafine particles in the upper tracheobronchial tree: a comparative study between approximate and realistic respiratory tract models. Comput. Methods Biomech. Biomed. Eng. 24, 1125–1135.
Dong, J., Shang, Y., Tian, L., Inthavong, K., Qiu, D., Tu, J., 2019. Ultrafine particle deposition in a realistic human airway at multiple inhalation scenarios. Int. J. Numer. Method Biomed. Eng. 35, e3215.
Farghadan, A., Poorbahrami, K., Jalal, S., Oakes, J.M., Coletti, F., Arzani, A., 2020. Particle transport and deposition correlation with near-wall flow characteristic under inspiratory airflow in lung airways. Comput. Biol. Med. 120, 103703.
Feng, Y., Kleinstreuer, C., 2014. Micron-particle transport, interactions and deposition in triple lung-airway bifurcations using a novel modeling approach. J. Aerosol Sci. 71, 1–15.
Fletcher, D.F., Chaugule, V., Gomes dos Reis, L., Young, P.M., Traini, D., Soria, J., 2021. On the use of computational fluid dynamics (CFD) modelling to design improved dry powder inhalers. Pharm. Res. 38, 277–288.
Ghalati, P.F., Keshavarzian, E., Abouali, O., Faramarzi, A., Tu, J., Shakibafard, A., 2012. Numerical analysis of micro-and nano-particle deposition in a realistic human upper airway. Comput. Biol. Med. 42, 39–49.
Gorji, T.B., Fatouraee, N., Mozaffari, A., 2013. Numerical simulation of transport and deposition of micro-particles in two-phase flow in a human upper airway model from CT images. Int. J. Exp. Comput. Biomech. 2, 171–188.
Grassia, P.S., Hinch, E.J., Nitsche, L.C., 1995. Computer simulations of Brownian motion of complex systems. J. Fluid Mech. 282, 373–403.
Gu, X., Wen, J., Wang, M., Jian, G., Zheng, G., Wang, S., 2019. Numerical investigation of unsteady particle deposition in a realistic human nasal cavity during inhalation. Exp. Comput. Multiph. Flow 1, 39–50.
Hou, L., Luby-Phelps, K., Lanni, F., 1990. Brownian motion of inert tracer macromolecules in polymerized and spontaneously bundled mixtures of actin and filamin. J. Cell Biol. 110, 1645–1654.
Huang, F., Zhu, Q., Zhou, X., Gou, D., Yu, J., Li, R., Tong, Z., Yang, R., 2021. Role of CFD based *in silico* modelling in establishing an *in vitro-in vivo* correlation of aerosol deposition in the respiratory tract. Adv. Drug Deliv. Rev. 170, 369–385.
Inthavong, K., Ge, Q., Se, C.M., Yang, W., Tu, J., 2011a. Simulation of sprayed particle deposition in a human nasal cavity including a nasal spray device. J. Aerosol Sci. 42, 100–113.

Inthavong, K., Zhang, K., Tu, J., 2011b. Numerical modelling of nanoparticle deposition in the nasal cavity and the tracheobronchial airway. Comput. Methods Biomech. Biomed. Eng. 14, 633–643.
Islam, M.S., Larpruenrudee, P., Hossain, S.I., Rahimi-Gorji, M., Gu, Y., Saha, S.C., Paul, G., 2021a. Polydisperse aerosol transport and deposition in upper airways of age-specific lung. Int. J. Environ. Res. Public Health 18, 6239.
Islam, M.S., Larpruenrudee, P., Paul, A.R., Paul, G., Gemci, T., Gu, Y., Saha, S.C., 2021b. SARS CoV-2 aerosol: how far it can travel to the lower airways? Phys. Fluids 33, 061903.
Islam, M.S., Larpruenrudee, P., Saha, S.C., Pourmehran, O., Paul, A.R., Gemci, T., Collins, R., Paul, G., Gu, Y., 2021c. How severe acute respiratory syndrome coronavirus-2 aerosol propagates through the age-specific upper airways. Phys. Fluids 33, 081911.
Kadota, K., Matsumoto, K., Uchiyama, H., Tobita, S., Maeda, M., Maki, D., Kinehara, Y., Tachibana, I., Sosnowski, T.R., Tozuka, Y., 2022. *In silico* evaluation of particle transport and deposition in the airways of individual patients with chronic obstructive pulmonary disease. Eur. J. Pharm. Biopharm. 174, 10–19.
Kaur, I.P., Bhandari, R., Bhandari, S., Kakkar, V., 2008. Potential of solid lipid nanoparticles in brain targeting. J. Control. Release 127, 97–109.
Kim, C.S., Iglesias, A.J., 1989. Deposition of inhaled particles in bifurcating airway models: I. Inspiratory deposition. J. Aerosol Med. 2, 1–14.
Kleinstreuer, C., Zhang, Z., Donohue, J., 2008. Targeted drug-aerosol delivery in the human respiratory system. Annu. Rev. Biomed. Eng. 10, 195–220.
Kolanjiyil, A.V., Kleinstreuer, C., 2019. Modeling airflow and particle deposition in a human acinar region. Comput. Math. Methods Med. 2019, 5952941.
Kong, F.Y., Zhang, J.W., Li, R.F., Wang, Z.X., Wang, W.J., Wang, W., 2017. Unique roles of gold nanoparticles in drug delivery, targeting and imaging applications. Molecules 22, 1445.
Koullapis, P., Kassinos, S.C., Muela, J., Perez-Segarra, C., Rigola, J., Lehmkuhl, O., Cui, Y., Sommerfeld, M., Elcner, J., Jicha, M., 2018. Regional aerosol deposition in the human airways: the SimInhale benchmark case and a critical assessment of *in silico* methods. Eur. J. Pharm. Sci. 113, 77–94.
Kreuter, J., 1991. Nanoparticle-based dmg delivery systems. J. Control. Release 16, 169–176.
Lee, W.H., Loo, C.Y., Traini, D., Young, P.M., 2015. Inhalation of nanoparticle-based drug for lung cancer treatment: advantages and challenges. Asian J. Pharm. Sci. 10, 481–489.
Lintermann, A., Schröder, W., 2017. Simulation of aerosol particle deposition in the upper human tracheobronchial tract. Eur. J. Mech. B Fluids 63, 73–89.
Longest, P.W., Holbrook, L.T., 2012. *In silico* models of aerosol delivery to the respiratory tract—development and applications. Adv. Drug Deliv. Rev. 64, 296–311.
Longest, P.W., Xi, J., 2007. Effectiveness of direct Lagrangian tracking models for simulating nanoparticle deposition in the upper airways. Aerosol Sci. Technol. 41, 380–397.
Mangal, S., Gao, W., Li, T., Zhou, Q.T., 2017. Pulmonary delivery of nanoparticle chemotherapy for the treatment of lung cancers: challenges and opportunities. Acta Pharmacol. Sin. 38, 782–797.
Mansour, H.M., Rhee, Y.S., Wu, X., 2009. Nanomedicine in pulmonary delivery. Int. J. Nanomed. 4, 299.
Massarotti, N., Mauro, A., Mohamed, S., Romano, M.R., 2021. Air contamination inside an actual operating room due to ultrafine particles: an experimental-numerical thermo-fluid dynamic study. Atmos. Environ. 249, 118155.
Morsi, S., Alexander, A., 1972. An investigation of particle trajectories in two-phase flow systems. J. Fluid Mech. 55, 193–208.
Mutuku, J.K., Chen, W.H., 2018. Flow characterization in healthy airways and airways with chronic obstructive pulmonary disease (COPD) during different inhalation conditions. Aerosol Air Qual. Res. 18, 2680–2694.
Nahar, K., Gupta, N., Gauvin, R., Absar, S., Patel, B., Gupta, V., Khademhosseini, A., Ahsan, F., 2013. *In vitro, in vivo* and *ex vivo* models for studying particle deposition and drug absorption of inhaled pharmaceuticals. Eur. J. Pharm. Sci. 49, 805–818.
Poorbahrami, K., Oakes, J.M., 2019. Regional flow and deposition variability in adult female lungs: a numerical simulation pilot study. Clin. Biomech. 66, 40–49.
Rahimi-Gorji, M., Gorji, T.B., Gorji-Bandpy, M., 2016. Details of regional particle deposition and airflow structures in a realistic model of human tracheobronchial airways: two-phase flow simulation. Comput. Biol. Med. 74, 1–17.
Rahman, M., Zhao, M., Islam, M.S., Dong, K., Saha, S.C., 2022. Numerical study of nano and micro pollutant particle transport and deposition in realistic human lung airways. Powder Technol. 402, 117364.
Rahman, M.M., Zhao, M., Islam, M.S., Dong, K., Saha, S.C., 2021a. Aerosol particle transport and deposition in upper and lower airways of infant, child adult human lungs. Atmosphere 12, 1402.
Rahman, M.M., Zhao, M., Islam, M.S., Dong, K., Saha, S.C., 2021b. Aging effects on airflow distribution and micron-particle transport and deposition in a human lung using CFD-DPM approach. Adv. Powder Technol. 32, 3506–3516.
Rahman, M.M., Zhao, M., Islam, M.S., Dong, K., Saha, S.C., 2021c. Numerical study of nanoscale and microscale particle transport in realistic lung models with and without stenosis. Int. J. Multiph. Flow 145, 103842.
Ruge, C.A., Kirch, J., Lehr, C.M., 2013. Pulmonary drug delivery: from generating aerosols to overcoming biological barriers—therapeutic possibilities and technological challenges. Lancet Respir. Med. 1, 402–413.
Russo, F., Boghi, A., Gori, F., 2018. Numerical simulation of magnetic nano drug targeting in patient-specific lower respiratory tract. J. Magn. Magn. Mater. 451, 554–564.
Scherließ, R., Bock, S., Bungert, N., Neustock, A., Valentin, L., 2022. Particle engineering in dry powders for inhalation. Eur. J. Pharm. Sci., 106158
Shi, H., Kleinstreuer, C., Zhang, Z., 2007. Modeling of inertial particle transport and deposition in human nasal cavities with wall roughness. J. Aerosol Sci. 38, 398–419.
Shih, T.H., Liou, W.W., Shabbir, A., Yang, Z., Zhu, J., 1995. A new k-ϵ eddy viscosity model for high reynolds number turbulent flows. Comput. Fluids 24, 227–238.
Singh, R., Lillard, J.W., 2009. Nanoparticle-based targeted drug delivery. Exp. Mol. Pathol. 86, 215–223.
Singhal, C., Malhotra, N., Chauhan, N., Narang, S., Pundir, C., Narang, J., 2016. Hierarchical electrodeposition of methylene blue on ZnO nanocrystals thin films layered on SnO_2/F electrode for *in vitro* sensing of anti-thalassemic drug. Mater. Sci. Eng. C 62, 596–604.
Sohrabi, S., Wang, S., Tan, J., Xu, J., Yang, J., Liu, Y., 2017. Nanoparticle transport and delivery in a heterogeneous pulmonary vasculature. J. Biomech. 50, 240–247.
Sohrabi, S., Zheng, J., Finol, E.A., Liu, Y., 2014. Numerical simulation of particle transport and deposition in the pulmonary vasculature. J. Biomech. Eng. 136, 121010.
Sosnowski, T.R., 2018. Powder particles and technologies for medicine delivery to the respiratory system: challenges and opportunities. KONA Powder Part. J. 35, 122–138.
Sun, T., Zhang, Y.S., Pang, B., Hyun, D.C., Yang, M., Xia, Y., 2021. Engineered nanoparticles for drug delivery in cancer therapy. Nanomater. Neoplasms 31–142.
Sung, J.C., Pulliam, B.L., Edwards, D.A., 2007. Nanoparticles for drug delivery to the lungs. Trends Biotechnol. 25, 563–570.
Tash, M.A., Tavakol, M.M., Abouali, O., Ahmadi, G., 2019. Deposition of ellipsoidal fibers in nasal cavity: influence of non-creeping flow conditions. In: Proceedings of the Fluids Engineering Division Summer Meeting. American Society of Mechanical Engineers. V005T005A053.
Tian, G., Longest, P.W., Su, G., Hindle, M., 2011a. Characterization of respiratory drug delivery with enhanced condensational growth using an individual path model of the entire tracheobronchial airways. Ann. Biomed. Eng. 39, 1136–1153.
Tian, G., Longest, P.W., Su, G., Walenga, R.L., Hindle, M., 2011b. Development of a stochastic individual path (SIP) model for predicting the tracheobronchial deposition of pharmaceutical aerosols: effects of transient inhalation and sampling the airways. J. Aerosol Sci. 42, 781–799.
Tsuji, Y., 2007. Multi-scale modeling of dense phase gas–particle flow. Chem. Eng. Sci. 62, 3410–3418.
Uchechi, O., Ogbonna, J.D., Attama, A.A., 2014. Nanoparticles for dermal and transdermal drug delivery. Appl. Nanotechnol. Drug Deliv. 4, 193–227.
Vachhani, S., Kleinstreuer, C., 2021. Comparison of micron-and nano-particle transport in the human nasal cavity with a focus on the olfactory region. Comput. Biol. Med. 128, 104103.
Valiulin, S.V., Onischuk, A.A., Dubtsov, S.N., Baklanov, A.M., An'kov, S.V., Plokhotnichenko, M.E., Tolstikova, T.G., Dultseva, G.G., Rusinov, V.L., Charushin, V. N., 2021. Aerosol inhalation delivery of triazavirin in mice: outlooks for advanced therapy against novel viral infections. J. Pharm. Sci. 110, 1316–1322.
Weibel, E.R., 1963. Geometric and dimensional airway models of conductive, transitory and respiratory zones of the human lung. In: Morphometry of the Human Lung. Springer, pp. 136–142.
Willis, L., Hayes, D., Mansour, H.M., 2012. Therapeutic liposomal dry powder inhalation aerosols for targeted lung delivery. Lung 190, 251–262.
Xi, J., Berlinski, A., Zhou, Y., Greenberg, B., Ou, X., 2012. Breathing resistance and ultrafine particle deposition in nasal–laryngeal airways of a newborn, an infant, a child, and an adult. Ann. Biomed. Eng. 40, 2579–2595.
Xu, G., Yu, C., 1986. Effects of age on deposition of inhaled aerosols in the human lung. Aerosol Sci. Technol. 5, 349–357.
Yhee, J.Y., Im, J., Nho, R.S., 2016. Advanced therapeutic strategies for chronic lung disease using nanoparticle-based drug delivery. J. Clin. Med. 5, 82.
Yu, G., Zhang, Z., Lessmann, R., 1996. Computer simulation of the flow field and particle deposition by diffusion in a 3-D human airway bifurcation. Aerosol Sci. Technol. 25, 338–352.
Zhang, Z., Kleinstreuer, C., 2003. Computational thermodynamics analysis of vaporizing fuel droplets in the human upper airways. JSME Int. Journal Ser. B Fluids Therm. Eng. 46, 563–571.
Zhang, Z., Kleinstreuer, C., 2004. Airflow structures and nano-particle deposition in a human upper airway model. J. Comput. Phys. 198, 178–210.
Zhang, Z., Kleinstreuer, C., Kim, C.S., 2008. Airflow and nanoparticle deposition in a 16-generation tracheobronchial airway model. Ann. Biomed. Eng. 36, 2095–2110.
Zhao, J., Feng, Y., Fromen, C.A., 2020. Glottis motion effects on the particle transport and deposition in a subject-specific mouth-to-trachea model: a CFPD study. Comput. Biol. Med. 116, 103532.